Atomic scale simulations of ductile failure micromechanisms in nanocrystalline Cu at high strain rates

Avinash M. Dongare,[1,2] Arunachalam M. Rajendran,[3] Bruce LaMattina,[4] Mohammed A. Zikry,[2] and Donald W. Brenner[1]

[1]*Department of Materials Science and Engineering, North Carolina State University, Engineering Building I, 911 Partners Way, Campus Box 7907, Raleigh, North Carolina 27695, USA*

[2]*Department of Mechanical and Aerospace Engineering, North Carolina State University, 3211 Broughton Hall, Campus Box 7910, 2601 Stinson Drive, Raleigh, North Carolina 27695, USA*

[3]*Department of Mechanical Engineering, University of Mississippi, 201-B Carrier Hall University, Mississippi 38677, USA*

[4]*U.S. Army Research Office, P.O. Box 12211, Research Triangle Park, North Carolina 27709, USA*

The micromechanisms related to ductile failure during dynamic loading of nanocrystalline Cu are investigated in a series of large-scale molecular-dynamics (MD) simulations. Void nucleation, growth, and coalescence are studied for a nanocrystalline Cu system with an average grain size of 6 nm under conditions of uniaxial tensile strain and triaxial tensile strain at a strain rate of 10^8 s^{-1}. The MD simulations of deformation of the nanocrystalline system under conditions of triaxial tensile stress show random nucleation of voids at grain boundaries and/or triple point junctions. The initial shape of the voids is nonspherical due to growth of the voids along the grain boundaries. Void growth is observed to occur by the creation of a shell of disordered atoms around the voids and not by nucleation of dislocations from the void surface. Void coalescence occurs by the shearing of the disordered regions in between the voids. The nucleation and growth of voids result in the relaxation of tensile stresses, after which growth of the voids is slower. The slower growth is accompanied by recrystallization of the surrounding disordered regions resulting in near-spherical shapes of the voids.

I. INTRODUCTION

Failure in ductile metals is initiated by extensive plastic deformation followed by nucleation, growth, and coalescence of voids. Uniaxial tension test experiments lead to failure (cup-cone fracture) after the material undergoes necking, during which the stress state transitions from uniaxial stress state to a triaxial stress state.[1] Nucleation of voids occurs during this triaxial state of stress. The voids grow and coalesce to form a crack surface resulting in subsequent failure. Failure of metals under dynamic loading conditions (spallation) is also attributed to the nucleation, growth, and coalescence of voids.[2] Plate impact experiments are typically used to study the dynamic properties of materials under extreme tensile conditions. A flyer plate is impacted on to a target plate at a very high velocity, which generates a planar shock. Compressive waves are generated in the projectile and the target plate which reach the rear surface and reflect as tensile waves. The reflected tensile waves meet at a planar region within the target to produce a triaxial stress state under conditions of uniaxial strain.[3] The interaction of reflected waves results in the simultaneous nucleation of multiple voids in this region. The voids grow until they interact with each other and coalesce to form microscopic cracks. Spallation failure therefore results in the formation of a microscopic crack on a well-defined plane (spall plane) parallel to the rear surface. Failure results in a slab of detached material being ejected from the back surface of the material. Plate impact experiments typically result in peak strain rates of 10^5–10^6 s^{-1}.[4–6] Spallation experiments can also be carried out using short-pulse lasers wherein planar fracture results when the reflected tensile stress wave exceeds the dynamic tensile strength of the material. Shock loading using short (nanosecond) laser pulses leads to peak strain rates exceeding 10^7 s^{-1},[7–9] whereas use of ultrashort (femtosecond) laser pulses results in strain rates exceeding 10^8 s^{-1}.[10,11]

A considerable amount of research has been aimed at understanding and predicting material response to dynamic loading conditions. A better understanding of the deformation and failure mechanisms will enhance the development and improvement of materials for use in conditions subjected to impact/shock. Nanocrystalline metals, due to their enhanced strength and wear resistance, show significant promise in the development of materials for use in conditions subjected to impact/shock. The plastic deformation mechanisms in nanocrystalline metals depend on the interplay between dislocation and grain-boundary (GB) processes. The higher grain-boundary density as the grain size decreases results in an increase in yield strength as suggested by the Hall-Petch effect.[12] The increase in strength with decreasing grain size, however, reaches a maximum after which further decrease in the grain size (≤ 12 nm) can result in weakening of the metal due to grain-boundary sliding dominating the deformation behavior.[13–16] This weakening of the metal is referred to as the inverse Hall-Petch behavior.[17] Nanocrystalline metals with ultrafine grain sizes ($d \leq 30$ nm) have gained considerable attention due to their increased strengths during deformation at high strain rates (10^4 s^{-1}).[18] In addition, shock loading of ultrafine nanocrystalline Ni at speeds that are greater than the speed of sound limits the GB sliding mechanism and thus results in ultrahigh strength values.[19] Thus, the ability to limit the GB sliding processes by the use of ultrahigh strain rates opens up the possibility of creating ultrahard metals for use in conditions subjected to impact/shock loading.

The design of ultrahard materials, however, also requires a fundamental understanding of the failure mechanisms at

these high strain rates. There have been several experiments aimed at understanding the failure behavior of metals at high strain rates (10^5–10^6 s^{-1}) (Refs. 2 and 4–6) as well as ultrahigh strain rates (10^7–10^9 s^{-1}).[7,11,20] Impact loading of polycrystalline metals results in the nucleation of voids at grain boundaries. The mechanisms of void nucleation in polycrystalline metals are attributed to GB sliding and/or dislocation pileups during impact loading.[2] However, the mechanisms related to growth and coalescence of voids that lead to dynamic failure are not clearly understood. The lack of understanding can be attributed to the small time scales of these processes, which makes it difficult to identify and characterize these processes using experiments alone. Computer simulations, with their current capabilities, allow the study of these phenomena and can complement experiments in the design of new materials with superior strength. Most of the modeling of failure of ductile metals has been carried out using continuum models,[21–28] although these studies mostly address the mechanism of void growth and porosity. These studies typically use the Gurson-type models,[21] which assume spherical or cylindrical voids and that the dilation of the void-matrix aggregate is completely due to void growth. Although the void-growth process is modeled explicitly, very simplistic criteria are used to account for coalescence of the voids. In addition, most of these studies are for quasistatic ductile fracture and the dynamic failure mechanisms are less studied. A few models of spallation failure[29–32] have been proposed to describe the void-growth-based failure in metals during plate impact experiments. These models, however, have to include a number of assumptions/criteria for the mechanisms of nucleation, growth, and coalescence of voids, as well as the dependence of strain rate and microstructure on these mechanisms.

An attractive alternative to study the micromechanisms related to ductile failure at high strain rates is the use of the molecular-dynamics (MD) simulation because of its potential to provide the level of detail needed for the physical interpretation of experimental observations.[33] MD simulations of plastic deformation are typically carried out at strain rates $\geq 10^7$ s^{-1}. While these strain rates are higher than conventional strain rates in ballistic impact experiments (10^5–10^6 s^{-1}), these strain rates compare well with the strain rates achieved experimentally during shock loading of metals using lasers.[7–11,20] As a result, large-scale MD simulations have been employed to study the micromechanisms associated with void growth[34–36] and coalescence.[37,38] Most of these studies, however, have been carried out for single-crystal systems assuming a pre-existing spherical void and void growth is observed to proceed through heterogeneous nucleation of dislocations from the void surface. The nucleation of voids, however, is neglected in these simulations. In addition, the presence of high density of grain boundaries in nanocrystalline metals and the interplay between dislocation and grain-boundary-based processes may affect the micromechanisms responsible for nucleation, growth, and coalescence of voids in nanocrystalline systems. As a result, current research focuses on the understanding of the failure mechanisms of nanocrystalline metals at high strain rates.[39–41] MD simulations of the deformation of nanocrystalline metals under conditions of uniaxial and triaxial ex-
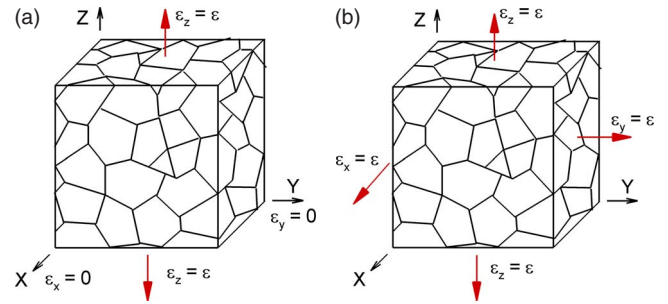

FIG. 1. (Color online) The setup of the constant strain simulations for conditions of (a) uniaxial strain in the Z direction and (b) triaxial strain for the nanocrystalline system.

pansion suggest the nucleation of voids at grain boundaries. The evolution of void growth and associated plasticity, however, is not explicitly discussed in these studies. In addition, the mechanisms of void coalescence are not addressed in detail.

The objective of this paper is to characterize, at the atomic scale, micromechanisms associated with the onset of ductile failure in a nanocrystalline metal at high strain rates. Void nucleation, growth, and coalescence are studied in nanocrystalline Cu with an average grain size of 6 nm that is subjected to tensile deformation under conditions of uniaxial and triaxial strains. The first study is focused on nanocrystalline Cu due to the availability of well-tested interatomic potentials[42–45] as well as the availability of a large amount of experimental data for failure at ultrahigh strain rates ($\geq 10^7$ s^{-1}).[7,20] The conditions of uniaxial expansion can be related to that experienced during spallation experiments, whereas that under triaxial expansion can be related to the necking phenomenon during ductile failure. The computational methods are presented in Sec. II. Nucleation mechanisms of nanoscale voids, the evolution of the void fraction and the associated plasticity are discussed in Sec. III for deformation under conditions of uniaxial strain, and in Sec. IV for deformation under conditions of triaxial strain.

II. COMPUTATIONAL METHODS

Large scale MD simulations are carried out to study the micromechanisms related to ductile failure in nanocrystalline Cu at high strain rates. A schematic of the simulation setup for the deformation conditions of uniaxial tensile strain and triaxial tensile strain are shown in Figs. 1(a) and 1(b), respectively. The Voter-Chen (VC) formulation[45] of the embedded atom method potential is used to describe the interatomic interactions for copper. The VC potential is well suited to describe deformation behavior for Cu as it provides a good description of the unstable and stable stacking fault energies, as well as the surface and grain-boundary energies.[46,47]

The initial nanocrystalline Cu system with an average grain size of 6 nm is created using the Voronoi construction method as suggested by Derlet and Van Swygenhoven.[48] Periodic boundary conditions are used in all the three directions. This procedure constructs a system with random grain orientations containing no textures and a grain-size distribu-
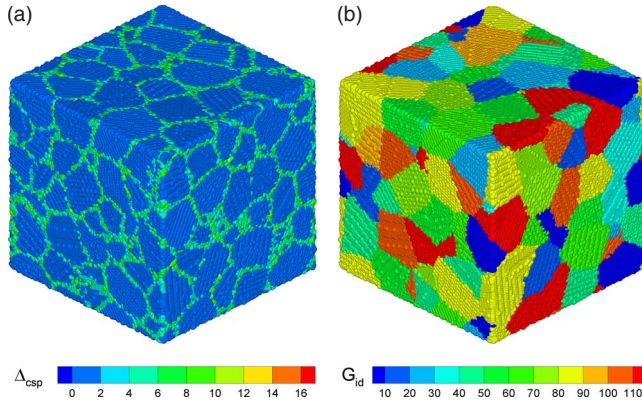
(a) (b)

FIG. 2. (Color online) The initial configuration of nanocrystalline Cu system with an average grain size of 6 nm. The system consists of approximately 1.2 million atoms arranged in 122 grains and each atom is colored according to the centrosymmetry parameter (Δ_{CSP}) values in (a) and according to the grain identity number (G_{id}) in (b).

tion close to a log-normal distribution.[49] The as-created system is first relaxed to have zero pressure and then equilibrated at 300 K for 100 ps. The density of the final configuration is calculated to be ~99% of the bulk density of copper. The centrosymmetry parameter (CSP) (Ref. [50]) is calculated for each atom using Eq. (1) during the simulations to identify local deformations in the face-centered-cubic (fcc) lattice,

$$\Delta_{CSP} = \sum_{i=1,6} |R_i + R_{i+6}|^2, \tag{1}$$

where R_i and R_{i+6} are the vectors or bonds corresponding to the six pairs of opposite nearest neighbors in the fcc lattice. The nanocrystalline Cu system with an average grain size of 6 nm and containing 122 grains (~1.2 million atoms) is shown in Fig. 2(a) with the atoms colored according to the CSP values (Δ_{CSP}). The contour scale for the CSP values in Fig. 2 is as follows: The black color (online=blue) corresponds to an fcc stacking, the gray (online=green) color represents grain boundaries and stacking faults, and the white (online=red) color represents a surface. One drawback of the CSP is that it becomes difficult to distinguish between stacking faults and grain boundaries. As a result, the common neighbor analysis (CNA) (Ref. [51]) is also used which allows characterization of dislocations separately from grain boundaries. In addition, a grain identity number (G_{id}) is assigned to each atom that defines the grain to which it belongs to in the nanocrystalline system. The identity of the grain for each atom allows the monitoring of the interdiffusion behavior of atoms in individual grains. The nanocrystalline Cu system with atoms colored according to the grain identity (G_{id}) number is shown in Fig. 2(b).

Elements of the atomic-level stress tensor are calculated as

$$\sigma_{\alpha\beta}(i) = -\frac{1}{\Omega_0} \left[\frac{1}{2} \sum_j F_{ij}^{\alpha} r_{ij}^{\beta} + M_i v_i^{\alpha} v_i^{\beta} \right], \tag{2}$$

where α and β label the Cartesian components, Ω_0 is the atomic volume, F_{ij} is the force on atom i due to atom j, M_i is

the mass of atom i, and v_i is the velocity of atom i. The strain (ε) calculated here is the engineering strain and the mean stress (σ_m) is calculated as

$$\sigma_m = (\sigma_x + \sigma_y + \sigma_z)/3, \tag{3}$$

where σ_x, σ_y, and σ_z are the stresses averaged over the entire system in the X, Y, and Z directions, respectively. An effective von Mises stress (σ_e) is calculated as

$$\sigma_e = \left\{ \frac{1}{2} [(\sigma_x - \sigma_y)^2 + (\sigma_y - \sigma_z)^2 + (\sigma_z - \sigma_x)^2 + 6(\sigma_{xy}^2 + \sigma_{yz}^2 + \sigma_{xz}^2)] \right\}^{1/2}. \tag{4}$$

Deformation under conditions of uniaxial expansion ($\varepsilon_x = \varepsilon_y = 0$ and $\varepsilon_z = \varepsilon$) is achieved at each time step by adjusting the z coordinate of all of the atoms using a scaling parameter. The coordinates of the atoms in the X and Y directions are not scaled, thus resulting in zero strains in the X and Y directions. Similarly, deformation under conditions of triaxial expansion ($\varepsilon_x = \varepsilon_y = \varepsilon_z = \varepsilon$) is achieved at each time step by adjusting the x, y, and z coordinates of all the atoms by a scaling parameter. The scaling parameter used for both the loading conditions is a constant and is chosen based on the time step and the initial system size to achieve the desired constant strain rate ($\dot{\varepsilon}$). The cell dimensions in the loading directions are adjusted accordingly at each step. The time step for all of the MD simulation runs is chosen to be 4 fs. The temperature was allowed to evolve during the deformation process.

III. TENSILE DEFORMATION OF NANOCRYSTALLINE CU UNDER CONDITIONS OF UNIAXIAL STRAIN

The results of MD simulations of the loading of nanocrystalline Cu with an average grain size of 6 nm under conditions of uniaxial strain ($\varepsilon_x = \varepsilon_y = 0$ and $\varepsilon_z = \varepsilon$) at a strain rate of 10^8 s^{-1} are discussed here. The stresses averaged over the entire system in the X, Y, and Z directions are plotted as functions of engineering strain (ε) in the Z direction in Fig. 3(a). The von Mises stress (σ_e) and the mean stress (σ_m) are plotted as functions of strain (ε) in Figs. 3(b) and 3(c), respectively.

Deformation under conditions of uniaxial tensile strain results in a triaxial state of tensile stress with $\sigma_x = \sigma_y$ and $\sigma_z \neq \sigma_x, \sigma_y$. The plots in Fig. 3 show three stages of deformation. The first stage corresponds to elastic deformation of the nanocrystalline system leading to a linear evolution of the curves for σ_x, σ_y, and σ_z up to the yield point given by A. The curves start to deviate from elastic behavior after this yield point due to GB sliding.[52] The shear stresses continue to increase during deformation till they reach a peak (as shown by point A′), after which the sliding behavior is accommodated by the nucleation of dislocations at the grain boundaries. The nucleation of dislocations results in a drop in the effective stress values. Continued deformation results in the nucleation of a void at point B in Fig. 3. A snapshot of a section of the system at a time just before the peak in the von Mises stress curve ($\varepsilon \sim 5\%$) is illustrated in Figs. 4(a)
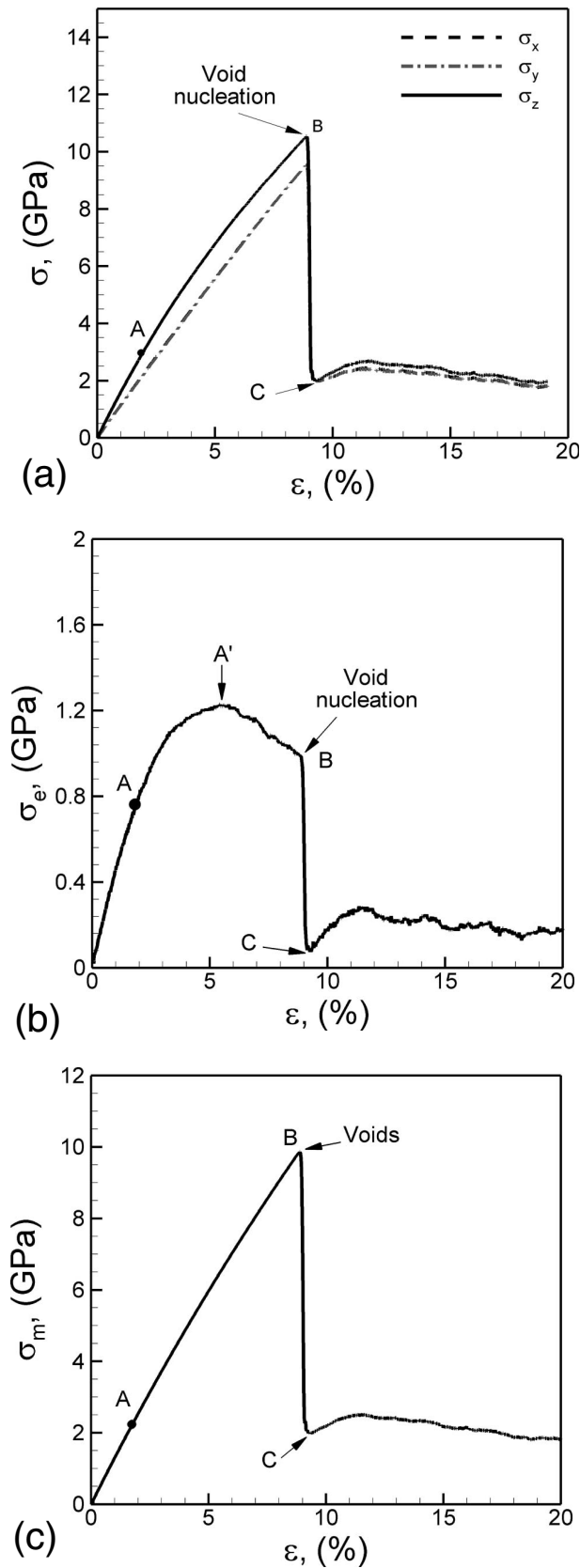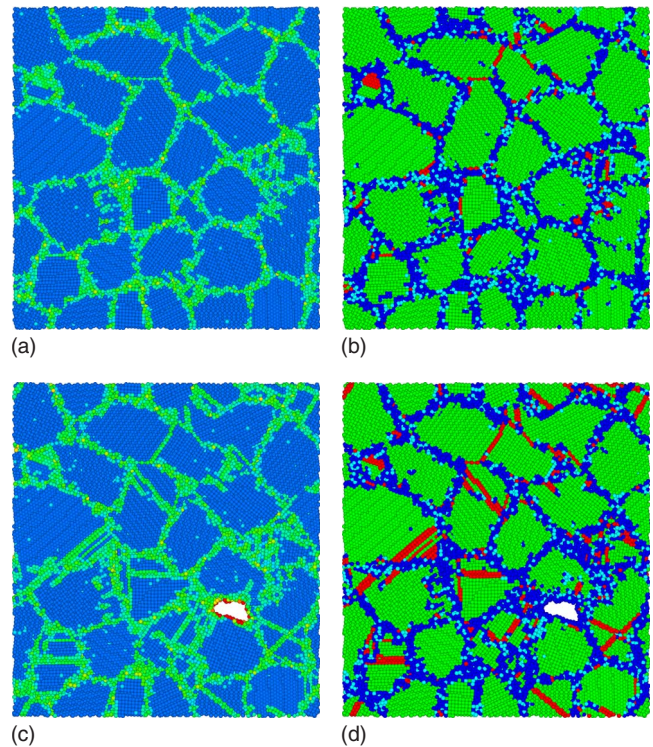
FIG. 4. (Color online) Snapshots of a section of the system at a time corresponding to peak von Mises stress with the atoms colored using (a) CSP and (b) CNA values. The snapshot of a section of the system at a time corresponding to nucleation of voids with the atoms colored using (c) CSP and (d) CNA values. The contour scale for CSP values is the same as used in Fig. 2.

and 4(b) with the atoms colored according to CSP and CNA values, respectively. The contour scale for the CSP values is the same as used in Fig. 2 with values as follows: the black (online=blue) colored atoms correspond to fcc ordered atoms, the gray (online=green) colored atoms correspond to grain boundaries or partial dislocations, and white (online =red) colored atoms correspond to atoms on a surface. The contour for the atoms colored according to their CNA values is as follows: the white (online=red) colored atoms represent local hexagonal close-packed order (stacking faults), the gray (online=green) atoms represent bulk fcc stacking, the dark gray atoms (online=light blue) represent a coordination greater than 12, and the black (online=blue) colored atoms represent a coordination of 12 other than fcc. A section of the system at the time corresponding to nucleation of a void is illustrated in Figs. 4(c) and 4(d) with the atoms colored according to CSP and CNA values, respectively. A single void is observed to nucleate at a grain-boundary interface between two grains at random for the loading conditions used in the simulations. It can also be seen that there is relatively little dislocation activity in Figs. 4(a) and 4(b), whereas the dislocation density increases significantly in Figs. 4(c) and 4(d). These snapshots confirm that GB sliding dominates deformation behavior at lower strains [up to point A′ in Fig. 3(b)] and dislocations dominate at higher strains.[52] However, no significant dislocation activity is observed in the grains surrounding the void. This indicates that void nucleation cannot be attributed to a dislocation pile-up process but rather re-

FIG. 3. Plots of (a) stresses in the *X*, *Y*, and *Z* directions, (b) von Mises effective stress (σ_e), and (c) mean stress (σ_m), as functions of engineering strain (ε) during tensile deformation under conditions of uniaxial strain at a strain rate ($\dot{\varepsilon}$) of 10^8 s^{-1}.

sults from the mechanical separation/sliding at the grain boundary. The sliding of the grain-boundary atoms generates high shear stresses which causes the separation of the system at the grain boundaries. As a result void growth occurs along the grain boundaries as shown in Figs. 4(c) and 4(d), and the shape of the void is observed to be nonspherical.

The nucleation of voids results in the relaxation of stresses as indicated by a sharp drop in the stresses in the X, Y, and Z directions as shown in Fig. 3(a). The stress state transitions to an almost hydrostatic stress condition ($\sigma_x \sim \sigma_y \sim \sigma_z$), resulting in a sharp drop in the effective stress values and mean stress values until a minimum is reached at point C as indicated by Figs. 3(b) and 3(c), respectively. The relaxation of tensile stresses at point C results in the stress state to transition back to that corresponding to uniaxial strain. The intermediate snapshots of a section of the system during these transitions in the stress state indicating the growth of the void are illustrated in Figs. 5(a)–5(f) with the atoms colored according to the CNA values. It can be seen from these snapshots that the voids nucleated initially grow along the grain boundary where the material is the weakest. This creation of the voids is accommodated by the shearing of the nearby atoms leading to the formation of a disordered shell of atoms around the void as shown in Fig. 5(a). Continued deformation increases the size of this shell of disordered atoms around the voids and the void shape changes to near spherical as shown in Figs. 5(b)–5(d). The larger disordered shell of atoms reduces the size of the crystalline regions in the grains surrounding the void suppressing the nucleation of dislocations into the neighboring grains from the void surface. Although a few dislocations are observed to propagate into the grains surrounding the void, most of the material surrounding the void consists of disordered atoms. Void growth is thus observed to occur by the shearing of the weakest regions, i.e., the disordered regions. The number of disordered atoms surrounding the void increases until the tensile stresses relax at point C in Fig. 3. This point C corresponds to the snapshot shown in Fig. 5(d). Continued deformation after point C results in the stress state to transition back to that corresponding to uniaxial strain conditions. This transition results in a slower growth rate of the void and is accompanied by the recrystallization of the surrounding disordered regions resulting in near-spherical shapes of the void. The growth rate of the void and the associated plasticity is discussed below.

The porosity or void fraction (V_f), defined as the ratio of the total volume of the voids (V_v) to the total volume (V_{tot}) of the system ($V_f = V_v / V_{tot}$), is calculated during the course of the simulations. To calculate the void fraction, a three-dimensional grid of cubic cells is superimposed over the atomic configuration and clusters of two or more contiguous empty cells are identified as voids.[53,54] The total volume of the empty cells (excluding single cells) divided by the total volume of the cells is calculated as the void fraction. The cell size (0.36 nm) is chosen so as to have at least several atoms in the cell for the case without any voids. The void fraction (V_f) is plotted as a function of time and engineering strain in Fig. 6(a). The evolution of void fraction can be described in two stages. The first stage (I) corresponds to a fast linear growth of individual voids under the conditions of hydro-
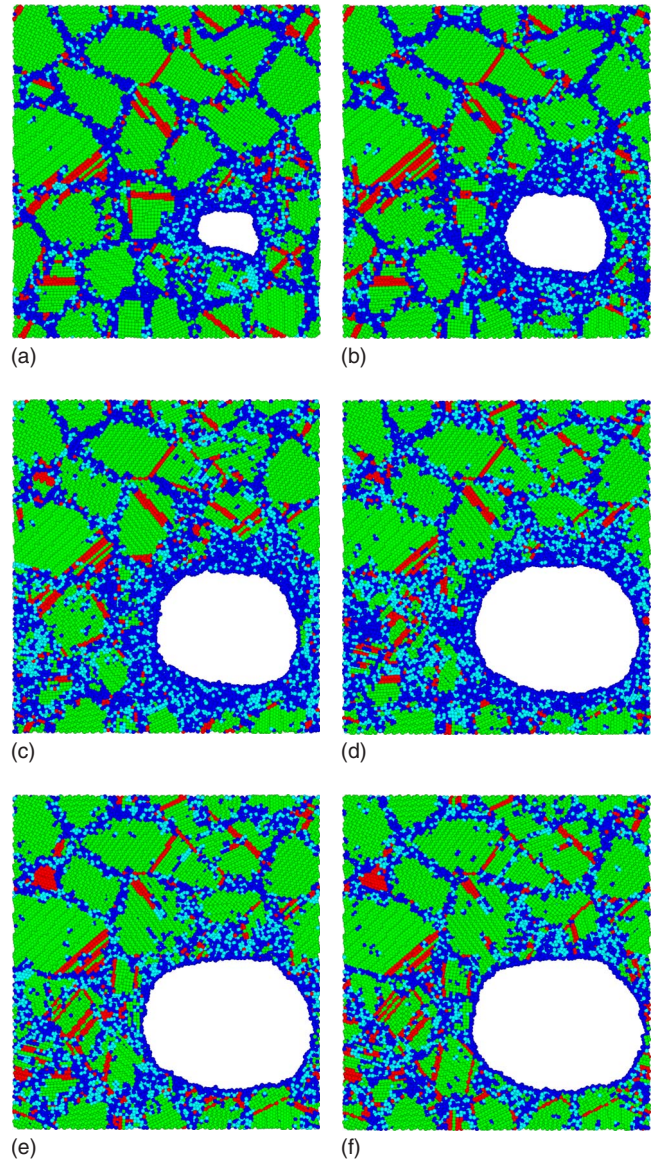

FIG. 5. (Color online) Snapshots of a section of the system at (a) 892 ps, (b) 896 ps, (c) 900 ps, (d) 904 ps, (e) 920 ps, and (d) 940 ps, showing the growth of the void under conditions of uniaxial tensile strain at a constant strain rate of 10^8 s^{-1}. The atoms are colored according to CNA values.

static stress ($\sigma_x \sim \sigma_y \sim \sigma_z$) by the creation and shearing of the disordered atoms surrounding the void. The transition from hydrostatic stress state to the stress state corresponding to uniaxial strain, after the minimum in tensile stresses is reached, results in the onset of the second stage (II) of void growth. The second stage (II) corresponds to a steady growth (slower) of the void accompanied by the recrystallization of the surrounding disordered regions resulting in near-spherical shapes of the void. The transition to steady growth occurs at a void fraction of $V_f \sim 0.055$ within 20 ps. Assuming a spherical void, this value of the void fraction corresponds to a growth of the void size (radius) from zero to 5.87 nm in 20 ps or a void-growth rate of ~ 0.3 nm/ps during stage I of ductile failure. Similarly the void-growth rate during stage II of ductile failure is calculated to be
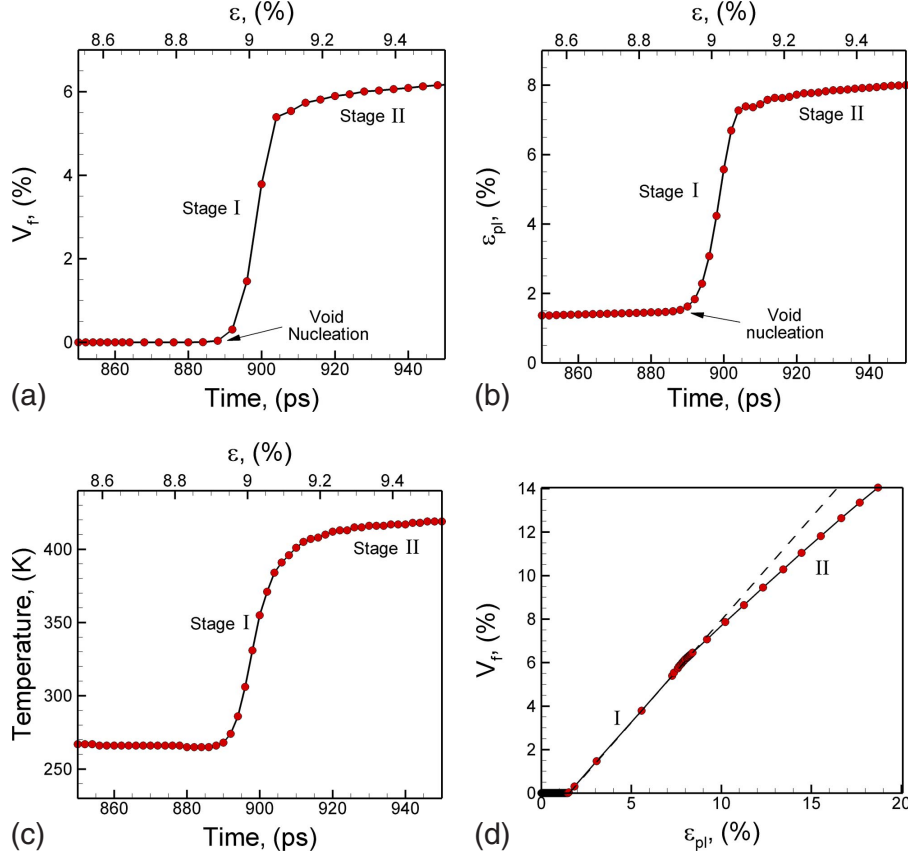
FIG. 6. (Color online) Evolution of (a) plastic strain, (b) void fraction, and (c) temperature as a function of time under conditions of uniaxial tensile strain at a constant strain rate of 10^8 s^{-1}. (d) Plot of void fraction as a function of plastic strain showing the linear projections of the two stages, (i) and (II), during tensile deformation under uniaxial strain of a nanocrystalline copper sample with an average grain size of 6 nm and a strain rate of 10^8 s^{-1}.

~ 0.0025 nm/ps, i.e., much slower as compared to stage I.

The plastic strain (ε_{pl}) is calculated using the general form of the Hooke's law,

$$\sigma_{ij} = \lambda e_{kk} \delta_{ij} + 2\mu e_{ij}, \tag{5}$$

where λ is Lame's constant and μ is the shear modulus (modulus of rigidity). At any step in the simulation, the total strain increment ($d\varepsilon = \dot{\varepsilon} dt$) in the system can be separated into an elastic component and a plastic component as

$$\dot{\varepsilon}_{tot} dt = \dot{\varepsilon}_{el} dt + \dot{\varepsilon}_{pl} dt. \tag{6}$$

The elastic part can be calculated using Eq. (5). For conditions of uniaxial strain, Eq. (5) reduces to $\sigma_x = \lambda \dot{\varepsilon} dt$, $\sigma_y = \lambda \dot{\varepsilon} dt$, and $\sigma_z = (\lambda + 2\mu) \dot{\varepsilon} dt$. The values for the Lame's constant (λ) and ($\lambda + 2\mu$) are calculated from the slope of the linear part of stress-strain curves in Fig. 3(a). The total plastic strain can then be calculated as

$$\dot{\varepsilon}_{pl} dt = \dot{\varepsilon}_{tot} dt - \left(\frac{\sigma_x + \sigma_y + \sigma_z}{3\lambda + 2\mu} \right). \tag{7}$$

The total plastic strain (ε_{pl}) is plotted as a function of time and engineering strain in Fig. 6(b). The initial plastic strain at which the void fraction is zero is attributed to GB sliding, after which the plastic strain follows an almost identical behavior as the void fraction. It should be noted that the tem-

perature is allowed to evolve during the deformation process. The plot of the average temperature in the system as a function of time and engineering strain is shown in Fig. 6(c). The initial expansion of the system results in a decrease in temperature which is attributed to the adiabatic cooling of the system. It can be seen from the plot that the temperature evolution follows the same two stages as the void fraction after the nucleation of the void. The nucleation of a void causes a sharp increase in the temperature followed by a transition to the third stage of a gradual increase in temperature. The plot of the evolution of temperature in the last two stages coincides with the plots of the evolution of void fraction and plastic strain. The temperature of the system reaches a value of ~ 450 K during stage II of void growth. The recrystallization of the disordered region around the void can thus be attributed to the higher temperature values during stage II of void growth. Thus, plastic deformation results in plastic work to be done in the system that results in the heating of the system. The evolution of void fraction is plotted as a function of the plastic strain in Fig. 6(d). The initial plastic strain at which the void fraction is zero is attributed to GB sliding and dislocation-induced plasticity, after which void growth follows an almost identical behavior as the plastic strain. This suggests that the nanocrystalline matrix is plastically incompressible and any local dilation is associated with either an elastic dilation or a change in porosity of the
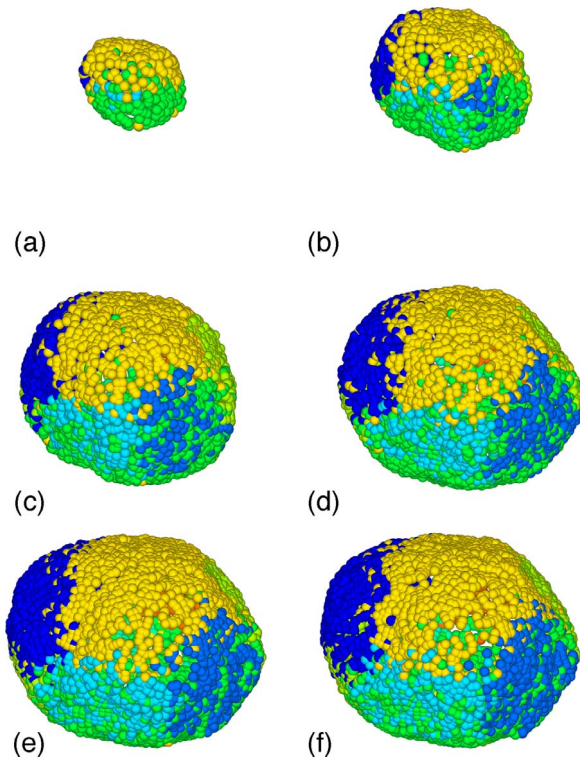
(a)

(b)

(c)

(d)

(e)

(f)

FIG. 7. (Color online) Snapshots of growth of the void at times of (a) 892 ps, $\varepsilon=8.95\%$, (b) 896 ps, $\varepsilon=8.99\%$, (c) 900 ps, $\varepsilon=9.03\%$, (d) 904 ps, $\varepsilon=9.07\%$, (e) 920 ps, $\varepsilon=9.23\%$, and (f) 940 ps, $\varepsilon=9.43\%$ under conditions of uniaxial tensile strain at a constant strain rate of 10^8 s^{-1}. The atoms are colored according to G_{id} number (color scale as in Fig. 2).

material. The size and shape of the void at intermediate times (corresponding to those in Fig. 5) are illustrated in Fig. 7. The void is obtained by showing only the atoms having a CSP value corresponding to a surface. The shape of the void is observed to be near spherical and confirms the experimental observations that the voids in ductile materials are generally observed to be almost spherical.

IV. TENSILE DEFORMATION OF NANOCRYSTALLINE Cu UNDER CONDITIONS OF TRIAXIAL STRAIN

The results of MD simulations of the tensile loading of nanocrystalline Cu under conditions of triaxial strain ($\varepsilon_1 = \varepsilon_2 = \varepsilon_3 = \varepsilon$) at a strain rate of 10^8 s^{-1} are discussed in this section. The initial nanocrystalline Cu system is the same as that used for loading under conditions of uniaxial strain. The deformation conditions of triaxial tensile strain result in a state of triaxial (hydrostatic) tensile stress ($\sigma_x = \sigma_y = \sigma_z$). The stresses averaged over the entire system in the X, Y, and Z directions are plotted as functions of engineering strain (ε) in Fig. 8(a). The engineering strain is the same as that in the X, Y, and Z directions, and hence can also be considered as the mean strain. The curves for σ_x, σ_y, and σ_z are linear almost to the point where void nucleation occurs. The mean stress (σ_m) and the von Mises effective stress (σ_e) are plotted as functions of engineering strain (ε) in Figs. 8(b) and 8(c), respectively. The von Mises stress curve is observed to fluc-
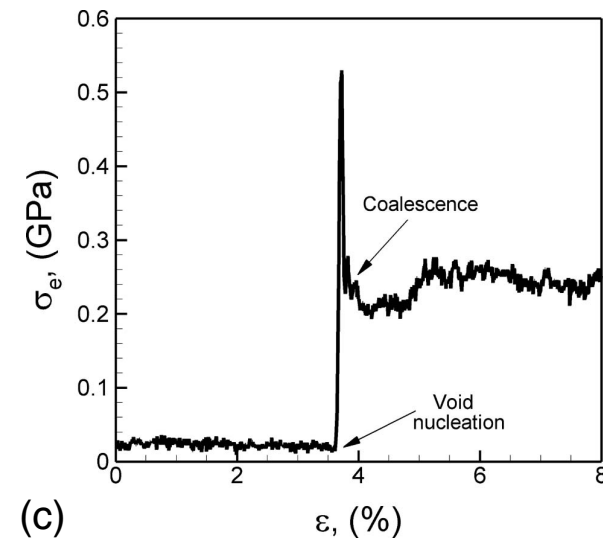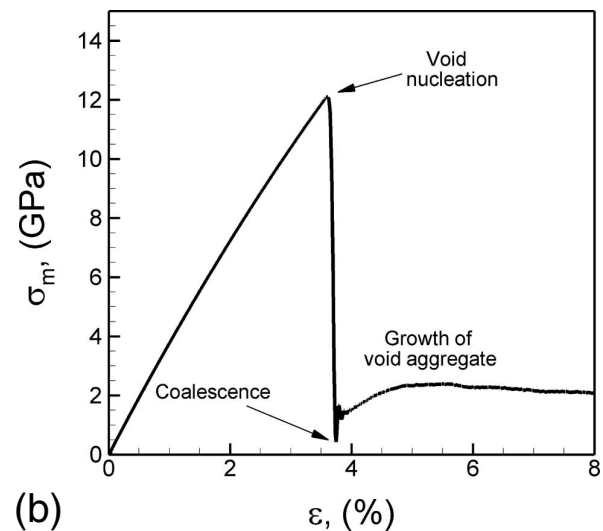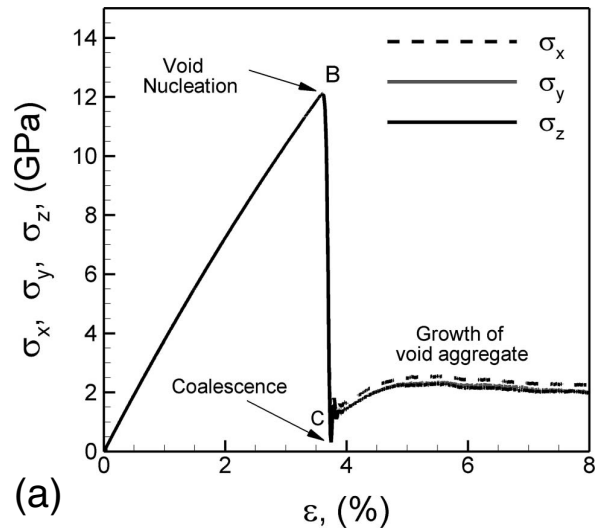

(a)

(b)

(c)

FIG. 8. Plots of (a) stresses in the X, Y, and Z directions, (b) mean stress (σ_m), and (c) von Mises stress (σ_e) as a function of engineering strain (ε) during tensile deformation under conditions of triaxial strain at a strain rate ($\dot\varepsilon$) of 10^8 s^{-1}.
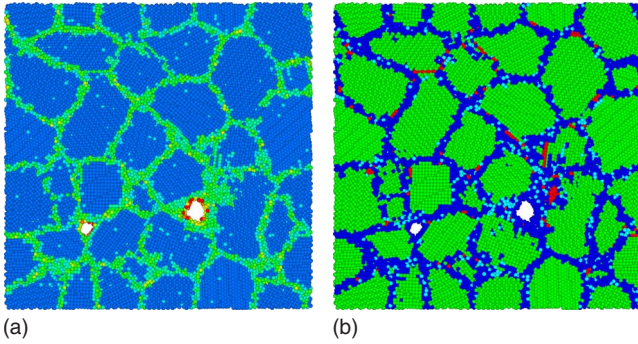
FIG. 9. (Color online) The snapshots of a section of the system at a time corresponding to nucleation of voids with the atoms colored using (c) CSP and (d) CNA values. The contour scale for the CSP values is the same as in Fig. 2.

tuate around very small values close to zero prior to nucleation of voids due to the hydrostatic stress state. Nucleation of voids results in a sharp peak in the von Mises stress values suggesting a deviation from the hydrostatic stress state. The peak value of the mean stress prior to nucleation of voids is greater under conditions of triaxial strain than that under conditions of uniaxial tensile strain. However, the strains at which voids nucleate are observed to be smaller under triaxial expansion as compared to those under uniaxial expansion.

Snapshots of a section of the system indicating the nucleation of voids are illustrated in Figs. 9(a) and 9(b), with the atoms colored according to CSP and CNA values, respectively. Two voids are observed to nucleate at the junction of three or four grains.[41] It can be seen from these snapshots that there is very little dislocation activity prior to nucleation of voids at the grain-boundary triple junctions. This clearly confirms that the nucleation of voids occurs due to mechanical separation/sliding of grains at the boundaries and not by dislocation pileups at the grain boundary. In addition, it can be seen that the number of dislocations observed prior to nucleation of voids is much lesser as compared to that observed during deformation under conditions of uniaxial expansion. Continued deformation results in the growth of the voids and the tensile stresses are observed to relax until a minimum is reached. This minimum in stresses coincides with to the coalescence of the two voids. Once the voids coalesce, continued deformation results in the deviation of the stress state from hydrostatic expansion as shown in Fig. 8(a). Intermediate snapshots of a section of the system indicating the nucleation, growth, and coalescence of the voids are illustrated in Figs. 10(a)–10(f) with the atoms colored according to CNA values. The contour scale is the same as used before. It can be seen from the snapshots that the growth of the voids occurs along the grain boundaries pushing more and more atoms into the surrounding grains. This creates a shell of disordered atoms around the voids. An increase in dislocation activity, however, is observed in the grains surrounding the disordered regions once the separation between the voids is less than the radius of the small void as illustrated in snapshot (c) in Fig. 10. Continued deformation results in the growth of the voids until they meet and coalescence as illustrated in Fig. 10(d). The growth of
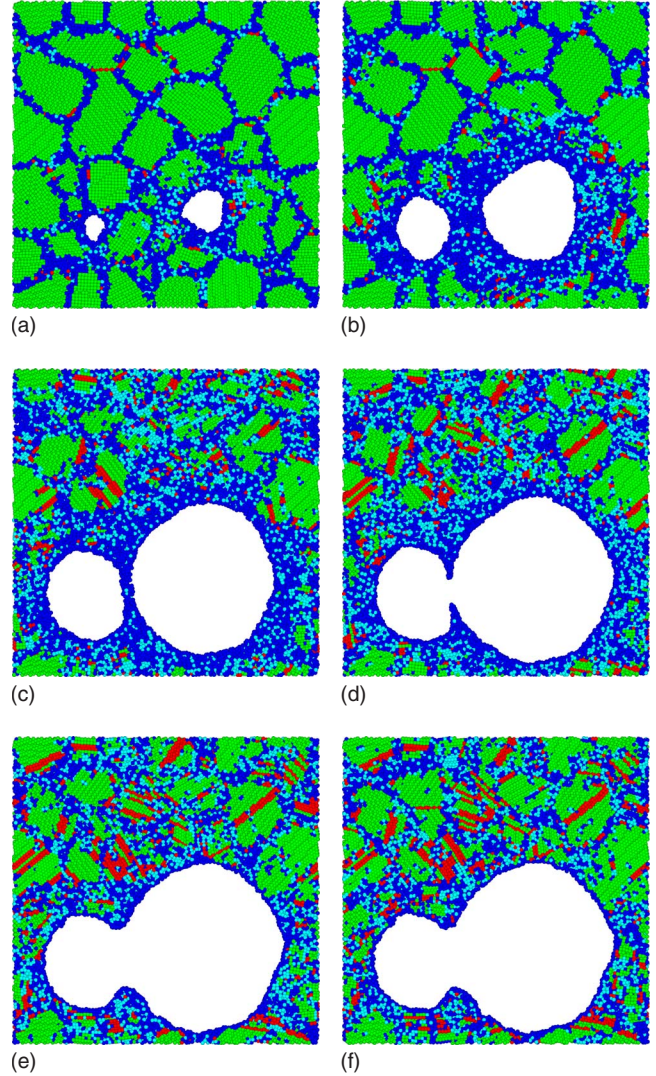

FIG. 10. (Color online) Snapshots of a section of the system at (a) 362 ps, $\varepsilon=3.61\%$ (b) 366 ps, $\varepsilon=3.63\%$ (c) 370 ps, $\varepsilon=3.67\%$ (d) 374 ps, $\varepsilon=3.75\%$, (e) 390 ps, $\varepsilon=3.91\%$, and (f) 400 ps, $\varepsilon=4.01\%$ under conditions of triaxial tensile strain at a constant strain rate of 10^8 s^{-1}. The atoms are colored according to CNA values.

the voids after coalescence is observed to be slower and is accompanied by the recrystallization of the surrounding disordered regions resulting in near-spherical shapes of the void as illustrated by snapshots (e) and (f) in Fig. 10.

The plastic strain increment ($d\varepsilon_{pl}=\dot{\varepsilon}_{pl}dt$) in each direction can be calculated by subtracting the elastic strain increment from the total strain increment as

$$\dot{\varepsilon}_{pl}dt = \dot{\varepsilon}_{\text{tot}}dt - \dot{\varepsilon}_{el}dt. \tag{8}$$

The evolution of plastic strain, void fraction, and average temperature of the system with time and strain is plotted in Figs. 11(a)–11(c), respectively. It can be seen that the plastic strain under hydrostatic expansion is significantly lower than that during uniaxial expansion. The initial plastic strain at which the void fraction is zero is attributed to dislocation induced plasticity and grain-boundary sliding. Once the voids nucleate, plastic strain follows an almost identical be-
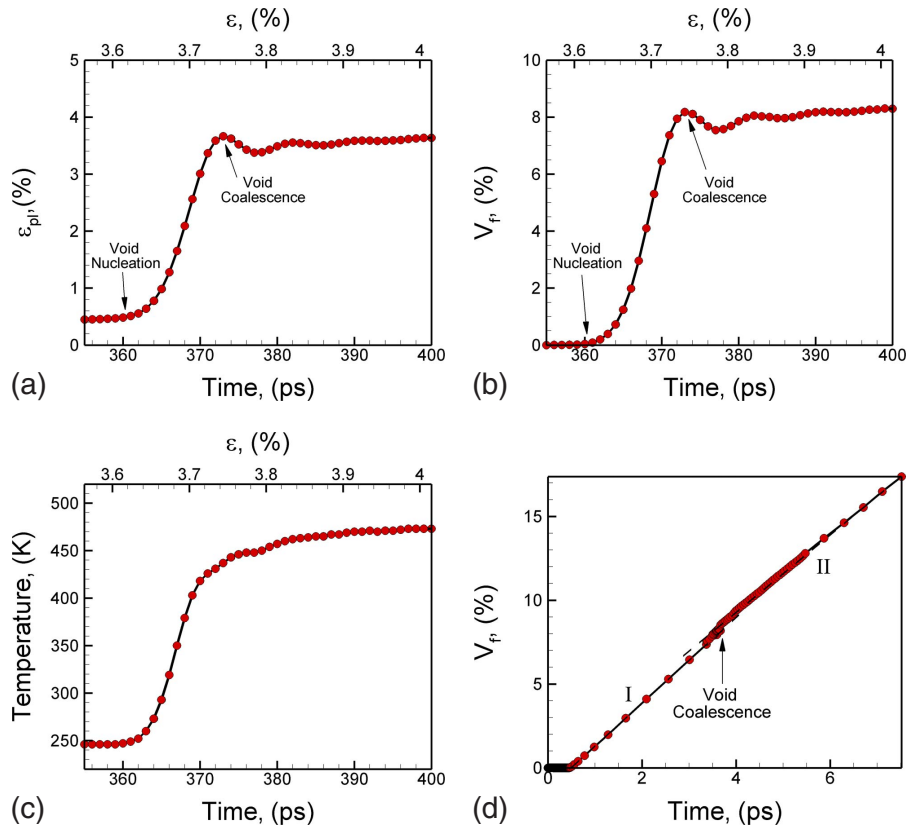
FIG. 11. (Color online) Evolution of (a) plastic strain, (b) void fraction, and (c) temperature as a function of time during tensile deformation under conditions of triaxial strain at a strain rate of 10^8 s^{-1}. The plot of void fraction as a function of plastic strain showing the linear projections of stage I and stage II of void growth is shown in (d).

havior as the void fraction, suggesting that the nanocrystalline matrix is plastically incompressible and any local dilation is associated with either an elastic dilation or a change in porosity of the material. The evolution of void fraction can be described in two stages. The first stage (I) corresponds to a fast growth of the individual voids under the conditions of hydrostatic stress until they meet and coalesce. The coalescence of the voids results in a deviation from the hydrostatic state of stress and leads to the onset of the second stage (II) of void growth. The second stage (II) growth is also linear with plastic strain but results in slower growth of the void accompanied by recrystallization of the surrounding disordered material. The evolution of the average temperature of the system is observed to be similar to that under conditions of uniaxial strain loading. The void fraction is plotted as a function of the plastic strain in Fig. 11(d). The recrystallization of disordered regions surrounding the voids can be attributed to the higher temperatures reached during stage II of void growth. It can be seen that the slope of the void fraction vs plastic strain curve changes very slightly during stage II of the growth. As a result, void fraction can be considered to vary linearly with plastic strain. The transition to slower growth occurs at a void fraction of $V_f \sim 0.08$. The size and shape evolution of voids at intermediate times are shown in Fig. 12. The void is obtained by showing only the atoms having a CSP value corresponding to a surface. It can be seen that the voids are near spherical as observed for the deformation conditions on uniaxial expansion.
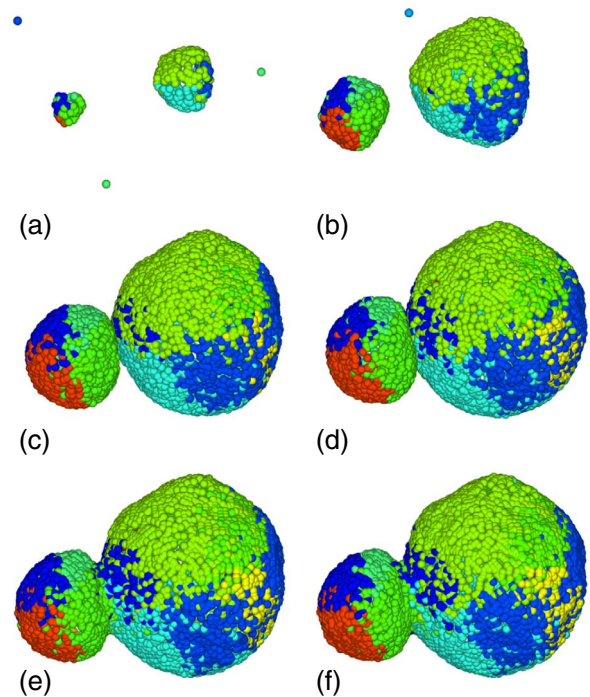

FIG. 12. (Color online) Evolution of voids at (a) 362 ps, $\varepsilon = 3.61\%$, (b) 366 ps, $\varepsilon = 3.63\%$, (c) 370 ps, $\varepsilon = 3.67\%$, (d) 374 ps, $\varepsilon = 3.75\%$, (e) 390 ps, $\varepsilon = 3.91\%$, and (f) 400 ps, $\varepsilon = 4.01\%$ under conditions of triaxial tensile strain at a constant strain rate of 10^8 s^{-1}. The atoms are colored according to G_{id}.

V. RELEVANCE TO SPALL BEHAVIOR

The results discussed above show that MD simulations are able to capture micromechanisms related to nucleation, growth, and coalescence of voids during dynamic loading conditions. The understanding of these mechanisms is important to predict the material response to failure under conditions of impact/shock loading, particularly spallation. Spallation failure typically occurs on a well-defined plane (defined as the spall plane) parallel to the rear surface resulting in a slab of detached material being ejected from the back surface of the material.[2] This spall plane experiences conditions of uniaxial tensile strain during shock loading, i.e., the only nonzero strain is in the shock-wave direction. Spallation experiments are typically used to study the spall strength of materials under extreme tensile conditions. The spall strength is defined as the maximum tensile stress the material is able to withstand under these conditions prior to failure. The strain rates generated during shock-wave propagation have a significant effect on the spall strength of the metal. The spall strength for copper (single and polycrystalline) is observed to increase slowly (0.7–3 GPa) with strain rate in the range $10^3 - 10^6$ s^{-1} whereas it increases rapidly (3–9 GPa) with strain rate in the range $10^7 - 2.5 \times 10^7$ s^{-1}.[7] The MD computational cell used here can be considered as being part of the material belonging to the incipient spall plane that experiences the triaxial tensile stress conditions generated due to the uniaxial strain conditions of loading. The plot of the mean stress as a function of effective strain under conditions of uniaxial tensile strain in Fig. 3(c) shows a peak tensile stress of 9.9 GPa at a strain rate of 10^8 s^{-1} prior to nucleation of voids. This value of the maximum mean tensile stress can be compared to the peak spall pressure during spallation experiments.[39] This calculated maximum tensile stress compares very well with the experimental values of ~9 GPa at a strain rate of 2.5×10^7 s^{-1}.[7] Thus MD simulations of nucleation, growth, and coalescence of voids can provide insights into the understanding of the failure response of the metal under dynamic loading conditions.

VI. CONCLUSIONS

Molecular-dynamics simulations are carried out to understand the micromechanisms related to ductile failure in nanocrystalline Cu at high strain rates. The MD simulations reported here suggest that the deformation of nanocrystalline Cu under conditions of uniaxial and triaxial expansion results in the nucleation of voids by mechanical separation/sliding at grain boundaries and/or triple point junctions in contrast to dislocation pileups observed in polycrystalline metals. One void is observed to nucleate under conditions of uniaxial expansion, whereas loading conditions of triaxial strain result in the nucleation of two voids for the same values of strain rate. The peak value of the mean stress is observed to be larger for triaxial strain loading as compared to that under uniaxial strain loading. The strain required to nucleate voids, however, is lower under conditions for triaxial strain loading as compared to uniaxial strain loading. The MD simulations also suggest void growth occurs by the shearing of the weakest regions, i.e., the disordered regions and not by nucleation of dislocations from the void surface at the nanocrystalline grain size considered. The void fraction is observed to vary linearly with plastic strain in two distinct stages. Stage I corresponds to a fast growth of the voids along the grain boundaries, thus pushing more and more atoms into the surrounding grains. This creates a shell of disordered atoms around the voids and further growth occurs by shearing of the disordered atoms resulting in nonspherical shapes. Stage I, when loading under uniaxial strain deformation, is accompanied by a transition in the triaxial state of stress from that corresponding to uniaxial strain to an almost hydrostatic stress state. On the other hand, stage I, under conditions of triaxial strain deformation, is accompanied by a deviation from a hydrostatic stress state. The onset of stage II of void growth occurs after a minimum is reached in the tensile stresses of the system. Stage II, under conditions of triaxial expansion, also coincides with the coalescence of voids. Stage II of void growth corresponds to a slower growth of the voids and is accompanied by the recrystallization of the surrounding disordered regions. The recrystallization of the disordered regions surrounding the voids is attributed to the higher temperatures reached during stage II of void growth. The results presented here indicate the validity of Gurson-type models to study void growth for nanocrystalline metals at high strain rates of deformation but need to include more detailed evolution laws for the void fraction.

ACKNOWLEDGMENTS

[1] J. F. Knott, *Fundamentals of Fracture Mechanics* (Butterworths, London, 1973).

[2] D. R. Curran, L. Seaman, and D. A. Shockey, Phys. Rep. **147**, 253 (1987).

[3] M. A. Meyers, *Dynamic Behavior of Materials* (Wiley-Interscience, New York, 1994).

[4] R. W. Minich, J. U. Cazamias, M. Kumar, and A. J. J. Schwartz, Metall. Mater. Trans. A **35**, 2663 (2004).

[5] J. M. Rivas, A. K. Zurek, W. R. Thissell, D. L. Tonks, and R. S. Hixson, Metall. Mater. Trans. A **31**, 845 (2000).

[6] J. P. Fowler, M. J. Worswick, A. K. Pilkey, and H. Nahme, Metall. Mater. Trans. A **31**, 831 (2000).

[7] E. Moshe, S. Eliezer, E. Dekel, A. Ludmirsky, Z. Henis, M. Werdiger, I. B. Goldberg, N. Eliaz, and D. Eliezer, J. Appl. Phys. **83**, 4004 (1998).

[8] G. I. Kanel, S. V. Razorenov, A. V. Utkin, V. E. Fortov, K.

Baumung, H. U. Karow, D. Rusch, and V. Licht, J. Appl. Phys. **74**, 7162 (1993).

[9] S. Eliezer, I. Gilath, and T. Bar-Noy, J. Appl. Phys. **67**, 715 (1990).

[10] H. Tamura, T. Kohama, K. Kondo, and M. Yoshida, J. Appl. Phys. **89**, 3520 (2001).

[11] E. Moshe, S. Eliezer, E. Dekel, Z. Henis, A. Ludmirsky, I. B. Goldberg, and D. Eliezer, J. Appl. Phys. **86**, 4242 (1999).

[12] G. F. Dieter, *Mechanical Metallurgy*, 3rd ed. (McGraw Hill, New York, 1986).

[13] H. Van Swygenhoven, Science **296**, 66 (2002).

[14] J. Schiotz and K. W. Jacobsen, Science **301**, 1357 (2003).

[15] V. Yamakov, D. Wolf, S. R. Phillpot, A. K. Mukherjee, and H. Gleiter, Philos. Mag. Lett. **83**, 385 (2003).

[16] K. S. Kumar, H. Van Swygenhoven, and S. Suresh, Acta Mater. **51**, 5743 (2003).

[17] D. Wolf, V. Yamakov, S. R. Phillpot, A. K. Mukherjee, and H. Gleiter, Acta Mater. **53**, 1 (2005).

[18] D. Jia, K. T. Ramesh, E. Ma, L. Lu, and K. Lu, Scr. Mater. **45**, 613 (2001).

[19] E. M. Bringa, A. Caro, Y. Wang, M. Victoria, J. M. McNaney, B. A. Remington, R. F. Smith, B. R. Torralva, and H. Van Swygenhoven, Science **309**, 1838 (2005).

[20] E. Dekel, S. Eliezer, Z. Henis, E. Moshe, A. Ludmirsky, and I. B. Goldberg, J. Appl. Phys. **84**, 4851 (1998).

[21] A. L. Gurson, ASME J. Eng. Mater. Technol. **99**, 2 (1977).

[22] V. Tvergaard and A. Needleman, Acta Metall. **32**, 157 (1984).

[23] A. Needleman, ASME J. Appl. Mech. **39**, 964 (1972).

[24] F. A. McClintok, ASME J. Appl. Mech. **35**, 363 (1968).

[25] J. R. Rice and D. M. Tracey, J. Mech. Phys. Solids **17**, 201 (1969).

[26] V. C. Orsini and M. A. Zikry, Int. J. Plast. **17**, 1393 (2001).

[27] W. M. Ashmawi and M. A. Zikry, Mater. Sci. Eng., A **343**, 126 (2003).

[28] W. M. Ashmawi and M. A. Zikry, Philos. Mag. **83**, 3917 (2003).

[29] P. F. Thomason, Acta Mater. **47**, 3633 (1999).

[30] A. M. Rajendran, M. A. Dietenberger, and D. J. Grove, J. Appl. Phys. **65**, 1521 (1989).

[31] F. R. Tuler and B. M. Butcher, Int. J. Fract. Mech. **4**, 431 (1968).

[32] T. W. Wright and K. T. Ramesh, J. Mech. Phys. Solids **56**, 336 (2008).

[33] D. W. Brenner, in *Nanostructured Materials: Processing, Properties, and Applications*, 2nd ed., edited by C. C. Koch (William Andrew Publishing, Norwich, NY, 2007), p. 293.

[34] E. T. Seppala, J. Belak, and R. E. Rudd, Phys. Rev. B **69**, 134101 (2004).

[35] A. M. Dongare, A. M. Rajendran, B. LaMattina, M. A. Zikry, and D. W. Brenner, *Nano- and Microscale Materials-Mechanical Properties and Behavior under Extreme Environments*, MRS Symposia Proceedings No. 1137 (Material Research Society, Pittsburgh, 2008), EE08-09-W10-09.R1.

[36] S. Traiviratana, E. M. Bringa, D. J. Bensona, and M. A. Meyers, Acta Mater. **56**, 3874 (2008).

[37] E. T. Seppala, J. Belak, and R. E. Rudd, Phys. Rev. B **71**, 064112 (2005).

[38] E. T. Seppala, J. Belak, and R. E. Rudd, Phys. Rev. Lett. **93**, 245503 (2004).

[39] A. Yu. Kuksin, V. V. Stegaĭlov, and A. V. Yanilkin, Phys. Solid State **50**, 2069 (2008).

[40] M. A. Meyers, S. Traiviratana, and V. A. Lubarda, JOM **61**, 35 (2009).

[41] R. E. Rudd and J. Belak, Comput. Mater. Sci. **24**, 148 (2002).

[42] M. S. Daw and M. I. Baskes, Phys. Rev. B **29**, 6443 (1984).

[43] S. M. Foiles, Phys. Rev. B **32**, 3409 (1985).

[44] R. A. Johnson, Phys. Rev. B **37**, 3924 (1988).

[45] A. F. Voter, in *Intermetallic Compounds: Principles and Practice*, edited by J. H. Westbrook and R. L. Fleischer (Wiley, New York, 1994), Vol. 77.

[46] J. A. Zimmerman, H. Gao, and F. F. Abraham, Modell. Simul. Mater. Sci. Eng. **8**, 103 (2000).

[47] Y. Mishin, M. J. Mehl, D. A. Papaconstantopoulos, A. F. Voter, and J. D. Kress, Phys. Rev. B **63**, 224106 (2001).

[48] P. M. Derlet and H. Van Swygenhoven, Phys. Rev. B **67**, 014202 (2003).

[49] S. Kumar, S. K. Kurtz, J. R. Banavar, and M. G. Sharma, J. Stat. Phys. **67**, 523 (1992).

[50] C. L. Kelchner, S. J. Plimpton, and J. C. Hamilton, Phys. Rev. B **58**, 11085 (1998).

[51] D. J. Honeycutt and H. C. Andersen, J. Phys. Chem. **91**, 4950 (1987).

[52] N. Q. Vo, R. S. Averback, P. Bellon, S. Odunuga, and A. Caro, Phys. Rev. B **77**, 134108 (2008).

[53] L. V. Zhigilei, D. S. Ivanov, E. Leveugle, B. Sadigh, and E. M. Bringa, Proc. SPIE **5448**, 505 (2004).

[54] E. Leveugle and L. V. Zhigilei, Appl. Phys. A: Mater. Sci. Process. **79**, 753 (2004).